

Kinetics and Intermediate Phases in Epitaxial Growth of Fe₃O₄ Films from Deposition and Thermal Reduction

Xiaozhe Zhang^{1,2}, Sen Yang¹, Zhimao Yang¹, Xiaoshan Xu²

¹School of Science, MOE Key Laboratory for Non-Equilibrium Synthesis and Modulation of Condensed Matter, Xi'an Jiaotong University, Xi'an 710049, ShaanXi, China

²Department of Physics and Astronomy, Nebraska Center for Materials and Nanoscience, University of Nebraska-Lincoln, Lincoln, NE 68588, USA

* Correspondence to: Xiaoshan Xu (xiaoshan.xu@unl.edu), Zhimao Yang (zymyang@xjtu.edu.cn)

PACS number(s): 68.35.-p, 69.49.-h, 68.55.-a, 68.60.-p

Abstract

We have studied the growth of Fe₃O₄ (111) epitaxial films on Al₂O₃ (001) substrates using a pulsed laser deposition / thermal reduction cycle using an α -Fe₂O₃ target. While direct deposition onto the Al₂O₃ (001) substrates results in an α -Fe₂O₃ epilayer, deposition on the Fe₃O₄ (111) surface results in a γ -Fe₂O₃ epilayer. The kinetics of the transitions between Fe₂O₃ and Fe₃O₄ were studied by measuring the time constants of the transitions. The transition from α -Fe₂O₃ to Fe₃O₄ via thermal reduction turns out to be very slow, due to the high activation energy. Despite the significant grain boundaries due to the mismatch between the unit cells of the film and the substrate, the Fe₃O₄ (111) films grown from deposition/thermal reduction show high crystallinity.

Introduction

Magnetite (Fe_3O_4), as one of the phases of iron oxides, has been of wide usage in, e.g., pigments, magnetic recording, and catalysis, due to their useful optical, magnetic, and chemical properties and the low cost. Additional applications are constantly being explored in Fe_3O_4 , particularly in molecular biology and spintronics, because of its bio-compatibility and special electronic structures respectively.¹⁻⁶

In the thermodynamic standard conditions, Fe_3O_4 is a metastable phase of iron oxide, which has an inverse spinel structure (space group $\text{Fd-}3\text{m}$).⁷ In Fe_3O_4 , the cubic unit cell contains eight formula units that can be written as $(\text{Fe}^{3+})_8[\text{Fe}^{3+}\text{Fe}^{2+}]_8\text{O}_{32}$. The Fe^{2+} and Fe^{3+} cations are located in the interstitial sites of oxygen anions sub-lattice. One cation site, occupied only by Fe^{3+} ions, is tetrahedrally coordinated to oxygen. The other site, occupied by equal numbers of Fe^{2+} and Fe^{3+} ions, is octahedrally coordinated to oxygen. Below $T_N \approx 860$ K, Fe_3O_4 is ferrimagnetic, in which the magnetic moments of the Fe^{3+} in two different sites cancels each other while the moments of the Fe^{2+} are aligned and form a spontaneous magnetization.⁸ The resistivity of Fe_3O_4 decreases when temperature increase, with a rapid change at $T_V \approx 120$ K, noted as the Verwey transition, which is often considered as a signature of the Fe_3O_4 phase.⁹⁻¹³

Great efforts have been devoted to preparing epitaxial Fe_3O_4 thin films using pulsed laser depositions, with a variety of target materials to begin with, including metal Fe,¹⁴ Fe_3O_4 ,^{9,15-18} and Fe_2O_3 .^{9-12,19} The iron oxide phase and oxygen stoichiometry of the films are sensitive to the growth conditions, especially temperature and background gas pressure.¹⁵ Therefore, thermodynamics and chemical reactions on the substrate are the key for the growth of Fe_3O_4 films, as also indicated by many studies on the transitions between iron oxide phases using surface characterizations.²⁰⁻³⁰ The

surface structures, including termination, reconstruction, and morphology, have been the focus of study.^{20–23,27} On the other hand, the kinetics of the transitions (time scale as a function of conditions) have seldom been systematically carried out, although the important energetic information can be extracted from the kinetics and the time scale itself is a critical factor both for studying or applying these transitions.

In this work, we studied the growth of Fe₃O₄ thin films using thermal reduction from the deposited Fe₂O₃ layers on Al₂O₃ (001) substrates. The time-resolved transitions between different phases of iron oxide were measured, using the reflection high energy electron diffraction (RHEED), around the phase boundaries. In particular, the transition from an α -Fe₂O₃ (001) layer to an Fe₃O₄ (111) layer show a long temperature-dependent time constant that follows the Arrhenius law with an activation energy of 2.3 ± 0.6 eV; the activation energy does not change significantly with the O₂ pressure while the time constant decreases with increasing pressure. These studies on kinetics of transitions between iron oxide phases at the surface are important for advancing our understanding on the response of the iron oxide surfaces to oxidation and reduction environments, which is critical in the application of iron oxides in heterogeneous catalysis, spintronics, and biomedicine.

Experimental

The film deposition was carried out on 0.2° miscut and one side polished sapphire Al₂O₃ (001) substrates using pulsed laser deposition (PLD), in 5×10^{-3} Torr O₂, with 600 °C substrate temperature. The substrates were heated by an infrared laser using an absorber attached to the back of the sample mechanically. Both the temperature of the absorber and the temperature of the substrate were monitored using two separate pyrometers. The uncertainty of the temperature measurements was about 50 °C. Before deposition, the substrates were annealed in base pressure

(lower than 1×10^{-7} Torr) at 600 °C for 30 minutes. Each deposition corresponds to an epilayer of approximately 2.5 nm. The target used for the deposition is Fe₂O₃ pellet prepared from high purity Fe₂O₃ powder, sintered at 1400 °C for 24 hours. An excimer laser (KrF, $\lambda = 248$ nm) was used at a fluence of 1.8 J/cm² and a repetition rate of 2 Hz. The target to substrate distance was kept at 5 cm. Thermal reduction of the α -Fe₂O₃ epilayers were carried out by heating the sample to high temperature in low O₂ pressure after the deposition of the target material. The transition between the iron oxide phases were studied using a time-resolved RHEED in which the images were taken automatically every 15 seconds. X-ray diffractions (XRD) were measured (θ -2 θ scan) using a Rigaku D/Max-B diffractometer, with a cobalt K- α source ($\lambda = 1.79$ Å). The rocking curves were measured using a Rigaku SmartLab with a copper K- α source ($\lambda = 1.54$ Å). Magneto optical Kerr effect (MOKE) on the iron oxide films was measured using a He-Ne laser (632.8 nm) and a photoelastic modulator, in a longitudinal geometry. Atomic force microscopy (AFM) was measured using a Bruker Dimension ICON at room temperature. Temperature dependent resistivity was measured in a Janis cryostat using a Van der Pauw geometry.

Results and Discussions

Structural analysis of the epitaxial layers

First, we examine the different iron oxide phases that appeared during the growth, including hematite (α -Fe₂O₃), maghematite (γ -Fe₂O₃), and magnetite (Fe₃O₄). Figure. 2 shows the RHEED patterns of the iron oxide layers as well as the Al₂O₃ (001) substrate, where Fig. 2(a), (c), (e), and (g) correspond to the condition in which the electron beam points along the Al₂O₃ <001> direction, while Fig. 2(b), (d), (f), and (h) correspond to the condition in which the electron beam points along the Al₂O₃ <120> direction; the two directions are perpendicular to each other. These phases,

as well as their epitaxial relations with the Al_2O_3 (001) substrate, are identified, according to the RHEED pattern, condition of appearance, and ex-situ characterizations. The structure of these phases and the epitaxial relations are depicted using models in Fig. 3 and summarized in Table I.^{7,31–33} Below, we show more detailed analysis.

Direct deposition of the target material onto the Al_2O_3 (001) surface resulted in the RHEED patterns displayed in Fig. 2(c) and (d), which are similar to those of the Al_2O_3 (001) surface, indicating a similar in-plane lattice structure. Using the pattern separation of the Al_2O_3 (001) as the calibration, one can calculate the in-plane lattice constant as $5.07 \pm 0.1 \text{ \AA}$, which matches the lattice constant of the $\alpha\text{-Fe}_2\text{O}_3$ (001) surface (see Table 1) within the experimental error. Since Al_2O_3 and Fe_2O_3 are isomorphic (R-3c corundum structure), it is understandable that the most stable iron oxide epilayer on Al_2O_3 (001) without thermal reduction, is $\alpha\text{-Fe}_2\text{O}_3$ (001). Therefore, we assign the structural phase that shows the RHEED patterns in Fig. 2(c) and (d) as $\alpha\text{-Fe}_2\text{O}_3$ (001). The epitaxial relation is Al_2O_3 (001) // $\alpha\text{-Fe}_2\text{O}_3$ (001) and Al_2O_3 [100] // $\alpha\text{-Fe}_2\text{O}_3$ [100]), as shown in Fig. 3(a). The corresponding reciprocal indices are marked accordingly.

The Fe_3O_4 (111) layer were obtained by thermally reducing the deposited Fe_2O_3 epilayer at high temperature. After the Fe_2O_3 epilayer underwent thermal reduction, we observed the RHEED patterns in Fig. 2(g) and (h), which also indicate a surface of triangular lattice. Assuming that a Fe_3O_4 (111) epilayer is on top of the Al_2O_3 (001) substrates and that the RHEED patterns observed in Fig. 2(g) and (h) are from the bulk reciprocal space projected onto the (111) surface, one can calculate the in-plane lattice constant as $5.93 \pm 0.05 \text{ \AA}$. For a normal Fe_3O_4 (111) surface, the in-plane lattice constant is 5.924 \AA , which is close to the observed value. Therefore, we assign the structural phase that shows these patterns as Fe_3O_4 (111). The epitaxial relation is Al_2O_3 (001)// Fe_3O_4 (111) and Al_2O_3 [100]// Fe_3O_4 [-211], as shown in Fig. 2. There is no obvious match

between the in-plane lattice constant of Al₂O₃ (001) and Fe₃O₄ (111), since the difference is more than 10%. To understand this epitaxial relation, we projected the Al₂O₃ unit cell and the Fe₃O₄ onto the (001) and (111) planes respectively, and overlapped the two unit cells, as shown in Fig. 3(b). The oxygen network appears to be overlapping well, which may be the reason for the epitaxial relation. The reciprocal indices of Fe₃O₄ (111) layer are marked in Fig. 2(g) and (h). Note that Fe₃O₄ has a face centered cubic (fcc) structure, so the lattice constant of the primitive cell of the (111) epilayer is $\frac{1}{\sqrt{2}}$ of the cubic lattice. Because of the fcc structure of the Fe₃O₄, only the reciprocal indices that have all-odd or all-even indices using the cubic indices are present, as shown in Fig. 2(g) and (h). Further verification of the Fe₃O₄ phase is found from ex-situ characterizations, such as x-ray diffraction, electric transport measurements, and magneto optical Kerr effect measurements (see the Subsection **Characterization of the Fe₃O₄ and γ -Fe₂O₃ films**).

The γ -Fe₂O₃ (111) epilayers were observed after deposition of the target material onto the Fe₃O₄ (111) surface. Among the iron oxide structural phases, γ -Fe₂O₃, another metastable phase of iron oxide at the thermodynamic standard conditions, has a similar structure with Fe₃O₄, as shown in Fig. 3(c). This structure can be represented as: (Fe³⁺)₈[Fe³⁺_{40/3}□_{8/3}]O₃₂ where □ denotes vacancy, in which eight Fe³⁺ atoms occupy tetrahedral sites while the remainder occupies octahedral sites.³⁴ In other words, it is a cation deficient spinel structure (space group P4₃32). Figure. 2(g) and (h) shows the RHEED pattern of the epilayers after the deposition of target material onto the Fe₃O₄ (111) surface. Interestingly, these patterns differ dramatically from those in Fig. 2(e) and (f), suggesting that the surface structure has a determinant effect on the structure of the epilayer. Since the target is Fe₂O₃ which contains only Fe³⁺, we expect mostly Fe³⁺ in the epilayer after the direct deposition. Based on the structural similarity and valence consideration, a γ -Fe₂O₃ (111) epilayer is expected after the direct deposition of the target material onto the Fe₃O₄ (111) surface.^{15,35} This

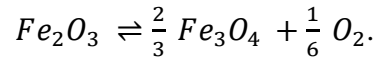
is confirmed using a combined characterizations: in-situ RHEED and ex-situ x-ray diffractions (see Subsection **Characterization of the Fe₃O₄ and γ -Fe₂O₃ films**).

Having identified the γ -Fe₂O₃ phase, we also note that the RHEED patterns of the γ -Fe₂O₃ (111) epilayer are not consistent with the bulk reciprocal space projected onto the (111) plane. The structure of γ -Fe₂O₃ has similar lattice constants with those of Fe₃O₄. But because the lattice is simple cubic, the primitive cell is actually smaller; one expect no systematic extinction for the diffraction. This means that the RHEED patterns of the γ -Fe₂O₃ (111) epilayer are supposed to have more streaks than those of the Fe₃O₄ (111) epilayers. In contrast, the observed RHEED patterns of the γ -Fe₂O₃ (111) in fact show less streaks. As shown Fig. in 2(e), in the $\langle 01-1 \rangle$ direction (Fig. 2(f)), there appears to be no (022), (0-2-2) streaks for the γ -Fe₂O₃ (111) surface. In addition, along the $\langle -211 \rangle$ direction, the (02-2) and (0-22) streaks are much weaker than the other diffraction streaks (marked as red arrow). In fact the RHEED patterns of the γ -Fe₂O₃ (111) epilayer is more consistent with a FeO (111) surface, which suggests a significant reconstruction at the γ -Fe₂O₃ (111) surface.¹⁵

The dependence of the structural phase on the structure of the beginning surface can be understood in terms of the interfacial energy. Since α -Fe₂O₃ and Al₂O₃ are isomorphic, the energy of the α -Fe₂O₃/Al₂O₃ interface is expected to be relatively lower than that of the γ -Fe₂O₃/Al₂O₃ interface. On the other hand, since γ -Fe₂O₃ and Fe₃O₄ have similar structures, the γ -Fe₂O₃/Fe₃O₄ interface is expected to have lower energy than that of the α -Fe₂O₃/Fe₃O₄ interface. Therefore, after the direct deposition, the α -Fe₂O₃/Al₂O₃ interface and the γ -Fe₂O₃/Fe₃O₄ interface are formed. In fact, a continuous change of epilayer structure from γ -Fe₂O₃ to Fe₃O₄ have been observed previously by changing the growth conditions.^{15,27,35}

Thermodynamics and the kinetics of the structural transitions

In order to study the kinetics of the $\text{Fe}_2\text{O}_3 \rightarrow \text{Fe}_3\text{O}_4$ transition, we first examined the boundary conditions between the phases using thermodynamic analysis. For both $\alpha\text{-Fe}_2\text{O}_3$ (001) and $\gamma\text{-Fe}_2\text{O}_3$ (111) epilayers, the conversion to a Fe_3O_4 (111) layer at high temperature, involves not only a change of crystal structure, but also a loss of oxygen, which can also be treated as thermal reduction. The condition for the $\text{Fe}_2\text{O}_3 \rightarrow \text{Fe}_3\text{O}_4$ transition, can be estimated according to change of Gibbs free energy ($\Delta_r G$) in the following reaction:



The $\Delta_r G$ for this reaction at certain temperature (T) and pressure (P) can be calculated from the Gibbs free energy at standard condition (ΔG^0) of Fe_2O_3 and Fe_3O_4 , using the relation

$$\Delta_r G = \frac{2}{3} \Delta_f G_{\text{Fe}_3\text{O}_4}^0 - \Delta_f G_{\text{Fe}_2\text{O}_3}^0 + \frac{1}{6} RT \ln \left(\frac{P}{P_0} \right), \text{ (see the supplementary materials}^{36}\text{),}$$

where P is the oxygen pressure and T is the temperature. The standard formation Gibbs free energy ($\Delta_f G_{\text{Fe}_2\text{O}_3}^0$ and $\Delta_f G_{\text{Fe}_3\text{O}_4}^0$) can be calculated using the corresponding formation enthalpy ($\Delta_f H^0$) and formation entropy ($\Delta_f S^0$), which can be assume as constants. Table II and Table III³⁷ show the values of $\Delta_f H^0$ and $\Delta_f S^0$. The boundary between the $\alpha\text{-Fe}_2\text{O}_3$ and the Fe_3O_4 phases is found by setting $\Delta_r G = 0$ and solving the relation between P and T . As shown in Fig. 4(c), the solid line is the calculated phase boundary of the Fe_2O_3 and Fe_3O_4 , consistent with the phase boundary calculated previously^{29,38}.

For the high pressure and low temperature region, $\alpha\text{-Fe}_2\text{O}_3$ phase is stable, while for the low pressure and high temperature region, the Fe_3O_4 phase is stable. The above thermodynamic analysis provides the information on the boundary between the bulk $\alpha\text{-Fe}_2\text{O}_3$ and Fe_3O_4 phases,

but not the rate of the transition (kinetics). Various time scales have been mentioned during the studies on the transition between iron oxide phases;²⁰⁻³⁰ however, a systematic study is lacking. Using the phase boundary in Fig. 4(c) as a guidance, we studied the kinetics of the $\alpha\text{-Fe}_2\text{O}_3 \rightarrow \text{Fe}_3\text{O}_4$ transition for an epilayer on the Al_2O_3 (001) substrate, by measuring the time evolution of the structure during the thermal reduction using the time-resolved RHEED.

Starting from the Al_2O_3 (001) substrate, we deposited the target material (~ 2.5 nm), which generates an $\alpha\text{-Fe}_2\text{O}_3$ (001) epilayer (see the supplementary materials³⁶). During the thermal reduction of $\alpha\text{-Fe}_2\text{O}_3$, we monitor the RHEED pattern with the incident electron along the $\langle 100 \rangle$ direction of the Al_2O_3 . Images of the RHEED patterns were saved every 15 seconds and integrated along the longer dimension of the diffraction streaks (see the supplementary materials³⁶). The evolution of the intensities of diffraction streaks is then plotted as a function of time. Figure. 4 (a) shows an example of RHEED intensity evolution at 930°C in 9.2×10^{-8} Torr O_2 . We found that the Fe_3O_4 (02-2) diffraction streaks slowly emerged between the diffraction streaks of $\alpha\text{-Fe}_2\text{O}_3$ (01) and (02), indicating the $\alpha\text{-Fe}_2\text{O}_3 \rightarrow \text{Fe}_3\text{O}_4$ transition. The intensity of the Fe_3O_4 streaks increases and starts to saturate after a certain time (see Fig. 4(b)). We fit the intensity (I) of the Fe_3O_4 streaks using the formula $I = I_0(1 - e^{-t/\tau})$, where t is time, I_0 is a saturation intensity, and τ is the time constant of the transition.

The time constant τ has been measured at different temperatures and the dependence is plotted in Fig. 4(d). When the temperature increases, τ decreases dramatically. We fit the temperature dependence of τ using the Arrhenius law, $\tau = \tau_0 e^{\frac{E_a}{kT}}$, where E_a is the activation energy and k is the Boltzmann constant. We repeated this study of time constant τ and activation energy at different O_2 pressure; the results are shown in Fig. 4(d). It is interesting that the activation energies

do not change significantly considering the experimental uncertainty (see Table IV), while τ_0 depends on the O_2 pressure dramatically.

In principle, the activation energy corresponds to the minimum energy barrier for the transition. For the $Fe_2O_3 \rightarrow Fe_3O_4$ transition, this energy barrier is related to breaking of the Fe-O bonds. The dissociation energy for a typical Fe-O bond is 4.2 eV however³⁹, which is about twice as much as the measured E_a (2.3 ± 0.6 eV on average). Therefore, it appears that at the surface, there are weaker Fe-O bonds that actually determine the E_a . In fact, the measured E_a value is close to the band gap energy of α - Fe_2O_3 .^{40,41} The band gap energy of α - Fe_2O_3 corresponds to the energy to excite an electron from O back to Fe, which can be understood as the breaking of the weakest possible link between the Fe and O atoms.

The observation that the activation energy is not significantly affected by the pressure, is not surprising, since the change of O_2 pressure is not supposed to affect the Fe-O bond energy significantly. In principle, higher O_2 pressure means the condition is closer to the boundary between the Fe_3O_4 and α - Fe_2O_3 phases; intuitively, the time constant τ_0 is expected to be larger. On the other hand, the experimental observations show that higher O_2 pressure actually makes the thermal reduction faster. We speculate a “fall-off” scenario of pressure dependent kinetics⁴²: because the α - $Fe_2O_3 \rightarrow Fe_3O_4$ is endothermic, when the pressure is lower, the heat transfer is expected to be slower, which may affect the rate of the transition.

The $Fe_3O_4 \rightarrow Fe_2O_3$ transition is more complex. At high temperature, the time constant is much smaller for the transition. After the thermal reduction, we decreased the substrate temperature to 600 °C and increased the background O_2 pressure to 5×10^{-3} Torr. The $Fe_3O_4 \rightarrow \alpha$ - Fe_2O_3 transition occurred within seconds, indicating a much smaller activation energy. Therefore, the rate of

oxidation is not determined by the energy scale to break the O-O bonds (5.2 eV),⁴³ which is not untypical for reactions on transition metal oxide surfaces.⁴⁴ On the other hand, at lower temperature, the transition is not only slow, but with different direct product (γ -Fe₂O₃). We carried out the annealing of the Fe₃O₄ films in one atmosphere O₂ at 250 °C for 4 hours. The RHEED pattern after that turned out to be similar to the ones in Fig. 4 (e) and (f) (see the supplementary materials³⁶). Ex-situ x-ray diffraction and magneto optical Kerr effect measurements indicates that the structure phase is γ -Fe₂O₃. (see the Subsection **Characterization of the Fe₃O₄ and γ -Fe₂O₃ films**).

Characterization of the Fe₃O₄ and γ -Fe₂O₃ films

To confirm the structural analysis of the epitaxial layer, we have characterized the Fe₃O₄ films (~30 nm) ex-situ using x-ray diffraction, atomic force microscopy, electric transport, and magneto-optical Kerr effect.

Figure. 5(a) shows the θ -2 θ scan of the Fe₃O₄ film grown by repeating the deposition/thermal reduction cycles. No impurity phases can be identified from the diffraction peaks. Figure. 5(b) is the close-up view of the (111) peaks, where the Laue oscillation is obvious, indicating flat surface of the film. Fitting the Laue oscillation with the consideration of background,⁴⁵ one can find the film thickness as 25 ± 1 nm. The inset shows the rocking curve of Fe₃O₄ (111) peak, for which the full-width-half-maximum (FWHM) is 0.14 degree, indicating a high crystallinity. One can estimate the size of the crystallites of the film using the peak width of the rocking curve and the θ -2 θ scans; the results show a size of 57 ± 1 nm along in-plane direction and 26 ± 1 nm along the out of plane direction (see the supplementary materials³⁶).

Figure. 6(a) shows the surface morphology of a Fe₃O₄ film measured using the atomic force microscopy. The surface of the film consists of domains separated by grooves of 1-2 nm deep. Despite this feature, the root mean square roughness of this film is 0.3 nm (Fig. S1(b)), confirming the flat surface indicated by the Laue oscillation observed in x-ray diffraction. Within the domains, the atomic terraces are observed (Fig. 6(c)), indicating again the high crystallinity. One of the origin of these grooves may be the unavoidable grain boundaries of the Fe₃O₄ films, when the epilayer has a larger unit cell than that of the substrate and the film nucleation occurs at different positions.⁴⁶⁻⁴⁸ For example, when a Fe₃O₄ film is deposited on a MgO substrate, similar mechanism generates anti-phase boundary because the lattice constant of Fe₃O₄ is about twice as much as that of MgO.⁴⁶⁻⁴⁸ The appearance of anti-phase boundary causes the deviation of transport properties and magnetic properties of the thin films from those of the bulk materials: the Verwey transition in the electric transport becomes less obvious with a decreased transition temperature; the magnetic coercivity is enhanced.⁴⁶⁻⁴⁸

To verify the Verwey transition in the Fe₃O₄ films, temperature dependence of the electrical resistance ($R - T$) has been measured between 50 and 300 K, as shown in Fig. 7(a). The Verwey transition temperature around 120 K is visible but not as clear as that in bulk,^{10,12,13,48} consistent with the significant domain boundaries. To highlight the Verwey transition, we have calculated effective activation energy (E_a^{eff}) using the relation $E_a^{eff} = \frac{d \ln R}{d(\frac{1}{kT})}$, where R is the resistance, k is the Boltzmann constant; the result is shown in Fig. 7(b). A clear anomaly is observed at 114 K, which is attributed to the Verwey transition.

Using the magneto-optical Kerr (MOKE) effect, we have measured the in-plane hysteretic behavior of the magnetization ($M - H$) of the Fe₃O₄ films at room temperature, as shown in Fig.

8. One can identify two features of the M-H loop here: a coercivity of ~ 270 Oe and a saturation field larger than 1000 Oe. Both of the coercivity and the saturation field are much larger than the bulk values, which may come from the effect of the significant grain boundaries.⁴⁶⁻⁴⁸

To verify the observation of the γ -Fe₂O₃ as an intermediate phase in the deposition, we annealed a Fe₃O₄ film (~ 30 nm) in one atmosphere O₂ at 250 °C for 4 hours.⁴⁹ The RHEED patterns of the annealed film turn from those in Fig. 2(g) and (h) to those in Fig. 2(e) and (f), indicating a phase transition (see the supplementary materials³⁶). As shown in Fig. 5(a), the x-ray diffraction spectrum of the annealed film is similar to that of the Fe₃O₄ film, except that the angles are systematically larger. The lattice constants calculated from the x-ray diffraction is 8.338 Å for the Fe₃O₄ film and 8.222 Å for the annealed Fe₃O₄ film, in agreement with the difference between the bulk values of Fe₃O₄ and γ -Fe₂O₃. Therefore, it appears that the annealed Fe₃O₄ film, as well as the layer observed in Fig. 2(e) and (f), are in fact the γ -Fe₂O₃ phase.

The hysteric of the magnetization ($M - H$) of the γ -Fe₂O₃ films is shown in the Fig. 8. One can see that the coercivity of the γ -Fe₂O₃ film is significantly less than that of the Fe₃O₄ film, which is in line with the results in the previous studies.¹⁵

Conclusion

By studying the growth of Fe₃O₄ (111)/Al₂O₃ (001) films using pulsed laser deposition and thermal reduction and studying the kinetics of the transitions between the iron oxide phases, we have found the activation energy for the α -Fe₂O₃→Fe₃O₄ transition is 2.3 ± 0.6 eV, corresponding to the weakest Fe-O bond to break at the surface. While the α -Fe₂O₃→Fe₃O₄ transition is slow due to the high activation energy, the Fe₃O₄→Fe₂O₃ transition is in general much faster and more complex. At high temperature, the oxidation of Fe₃O₄ is quick and results directly in the α -Fe₂O₃ phase; at

lower temperature, the oxidation of Fe_3O_4 is much slower and generates the intermediate $\gamma\text{-Fe}_2\text{O}_3$ phase. The Fe_3O_4 (111) films grown from thermal reduction show high crystallinity, even though films contain significant grain boundaries due to the larger mismatch between the in-plane unit cells of Al_2O_3 (001) and Fe_3O_4 (111).

Acknowledgement

This project was primarily supported by the National Science Foundation (NSF), DMR under Award DMR-1454618. Additional support (X. Z.) was from NSF, DMR under Award DMREF: SusChEM 1436385. Z.M.Y and S.Y. acknowledge the support from the National Science Foundation of China (NSFC No. 51272209, 51471125 and 51501140), the Shaanxi Province Science and Technology Innovation Team Project (2013KCT-05). X.Z. is grateful for the help from Jack Rodenburg and Shi Cao on the MOKE measurements.

References

- ¹ S.A. Wolf, D.D. Awschalom, R.A. Buhrman, M. Daughton, S. von Molna, M.L. Roukes, A.Y. Chtchelkanova, and D.M. Treger, *Science* **294**, 1488 (2001).
- ² J. Versluijs, M. Bari, and J. Coey, *Phys. Rev. Lett.* **87**, 026601 (2001).
- ³ J. Zlatanova and S.H. Leuba, *Biochem. Cell Biol.* **81**, 151 (2003).
- ⁴ S. Jain, *J. Appl. Phys.* **95**, 7237 (2004).
- ⁵ A. Fernández-Pacheco, J.M. De Teresa, J. Orna, L. Morellon, P.A. Algarabel, J.A. Pardo, M.R. Ibarra, C. Magen, and E. Snoeck, *Phys. Rev. B* **78**, 3 (2008).
- ⁶ I. Žutić, J. Fabian, and S. Das Sarma, *Rev. Mod. Phys.* **76**, 323 (2004).
- ⁷ L.W. Finger, R.M. Hazen, and A.M. Hofmeister, *Phys. Chem. Miner.* **13**, 215 (1986).
- ⁸ R.J. Harrison and A. Putnis, *Am. Mineral.* **81**, 375 (1996).
- ⁹ S.B. Ogale, K. Ghosh, R.P. Sharma, R.L. Greene, R. Ramesh, and T. Venkatesan, *Phys. Rev. B* **57**, 7823 (1998).
- ¹⁰ D.M. Phase, S. Tiwari, R. Prakash, A. Dubey, V.G. Sathe, and R.J. Choudhary, *J. Appl. Phys.* **100**, (2006).
- ¹¹ S. Tiwari, R. Prakash, R.J. Choudhary, and D.M. Phase, *J. Phys. D-Applied Phys.* **40**, 4943 (2007).
- ¹² R. Master, S. Tiwari, R.J. Choudhary, U.P. Deshpande, T. Shripathi, and D.M. Phase, *J. Appl. Phys.* **109**, 043502 (2011).
- ¹³ E.J.W. Verwey, *Nature* **144**, 327 (1939).
- ¹⁴ X. Liu, H. Lu, and M. He, *J. Phys. D. Appl. Phys.* **47**, 105004 (2014).
- ¹⁵ J.A. Moyer, S. Lee, P. Schiffer, and L.W. Martin, *Phys. Rev. B* **91**, 64413 (2015).

- ¹⁶ J.-A. Kim, S.-K. Lee, and S.-G. Yoon, *Sensors Actuators B Chem.* **204**, 622 (2014).
- ¹⁷ M.L. Paramês, J. Mariano, Z. Viskadourakis, N. Popovici, M.S. Rogalski, J. Giapintzakis, and O. Conde, *Appl. Surf. Sci.* **252**, 4610 (2006).
- ¹⁸ X.W. Li, A. Gupta, G. Xiao, and G.Q. Gong, *J. Appl. Phys.* **83**, 7049 (1998).
- ¹⁹ J. Yun, Y. Lee, W. Lee, C. Kim, and S. Yoon, *J. Mater Chem. C* **1**, 1977 (2013).
- ²⁰ A.R. Lennie, N.G. Condon, F.M. Leibsle, P.W. Murray, G. Thornton, and D.J. Vaughan, *Phys. Rev. B* **53**, 10244 (1996).
- ²¹ W. Weiss and M. Ritter, *Phys. Rev. B* **59**, 5201 (1999).
- ²² G.D. Waddill and O. Ozturk, *Surf. Sci.* **575**, 35 (2005).
- ²³ M. Xue, S. Wang, K. Wu, J. Guo, and Q. Guo, *Langmuir* **27**, 11 (2011).
- ²⁴ C. Schlueter, M. Lübbe, A.M. Gigler, and W. Moritz, *Surf. Sci.* **605**, 1986 (2011).
- ²⁵ S. Kaya, H. Ogasawara, and A. Nilsson, *Catal. Today* **240**, 184 (2015).
- ²⁶ E.C. Spencer, N.L. Ross, R.E. Olsen, B. Huang, A.I. Kolesnikov, and B.F. Wood, *Int. J. Thermophys.* **36**, 3 (2015).
- ²⁷ F.C. Voogt, T. Fujii, P.J.M. Smulders, L. Niesen, M.A. James, and T. Hibma, *Phys. Rev. B* **60**, 11193 (1999).
- ²⁸ T. Nagahama, Y. Matsuda, K. Tate, T. Kawai, N. Takahashi, S. Hiratani, Y. Watanabe, T. Yanase, and T. Shimada, *Appl. Phys. Lett.* **105**, (2014).
- ²⁹ C.H. Lanier, A.N. Chiaramonti, L.D. Marks, and K.R. Poeppelmeier, *Surf. Sci.* **603**, 2574 (2009).
- ³⁰ F. Bertram, C. Deiter, K. Pflaum, M. Suendorf, C. Otte, and J. Wollschla, **110**, 102208 (2011).
- ³¹ C. Pecharromán, T. González-Carreño, and J.E. Iglesias, *Phys. Chem. Miner.* **22**, 21 (1995).

- ³² L.W. Finger and R.M. Hazen, *J. Appl. Phys.* **51**, 5362 (1980).
- ³³ J. Lewis, D. Schwarzenbach, and H.D. Flack, *Acta Crystallogr. Sect. A* **38**, 733 (1982).
- ³⁴ R. Grau-Crespo, A.Y. Al-Baitai, I. Saadoune, and N.H. De Leeuw, *J. Phys. Condens. Matter* **22**, 255401 (2010).
- ³⁵ X.L. Huang, Y. Yang, and J. Ding, *Acta Mater.* **61**, 548 (2013).
- ³⁶ See Supplemental Material at <http://link.aps.org/supplemental/XXXX> for more detailed information.
- ³⁷ R.A. Robie and B.S. Hemingway, *Thermodynamic Properties of Minerals and Related Substances at 298.15 K and 1 Bar (105 Pascals) Pressure and at Higher Temperatures* (U.S. G.P.O. ; For sale by U.S. Geological Survey, Information Services, Washington; Denver, CO, 1995).
- ³⁸ G. Ketteler, W. Weiss, W. Ranke, and R. Schlögl, *Phys. Chem. Chem. Phys.* **3**, 1114 (2001).
- ³⁹ T.L. Cottrell, *The Strengths of Chemical Bonds* (Butterworths, London, 1958).
- ⁴⁰ S.S. Shinde, R. a Bansode, C.H. Bhosale, and K.Y. Rajpure, *J. Semicond.* **32**, 013001 (2011).
- ⁴¹ M.F. Al-Kuhaili, M. Saleem, and S.M.A. Durrani, *J. Alloys Compd.* **521**, 178 (2012).
- ⁴² C.H. Bamford, C.F.H. Tipper, and R.G. Compton, *Comprehensive Chemical Kinetics*. (Elsevier Pub. Co., Amsterdam; New York, 1969).
- ⁴³ S.W. Benson, *J. Chem. Educ.* **42**, 502 (1965).
- ⁴⁴ H.H. Kung, *Transition Metal Oxides : Surface Chemistry and Catalysis* (Elsevier ; Distributors for the U.S. and Canada, Elsevier Science Pub. Co., Amsterdam, The Netherlands; New York; New York, NY, U.S.A., 1989).
- ⁴⁵ H. Iida, T. Koizumi, Y. Uesu, K. Kohn, N. Ikeda, S. Mori, R. Haumont, P.-E. Janolin, J.-M. Kiat, M. Fukunaga, and Y. Noda, *J. Phys. Soc. Japan* **81**, 1 (2012).

⁴⁶ D.T. Margulies, F.T. Parker, M.L. Rudee, F.E. Spada, J.N. Chapman, P.R. Aitchison, and a E. Berkowitz, Phys. Rev. Lett. **79**, 5162 (1997).

⁴⁷ W. Eerenstein, T.T.M. Palstra, T. Hibma, and S. Celotto, Phys. Rev. B **66**, 201101 (2002).

⁴⁸ X.H. Liu, A.D. Rata, C.F. Chang, A.C. Komarek, and L.H. Tjeng, Phys. Rev. B **90**, 1 (2014).

⁴⁹ R. Dronskowski, Adv. Funtional Mater. **11**, 27 (2001).

Tables

Table I. The structures of the substrates and epitaxial orientations with different material during the deposition: Al₂O₃ (001), α -Fe₂O₃ (001), γ -Fe₂O₃ (111) and Fe₃O₄ (111).^{7,31-33}

Structure		Lattice constants (bulk, in Å)	Lattice constant (plane /in Å)	Epitaxial orientation
Al ₂ O ₃	R-3c (167)	a=4.7602, c=12.9933	(001), 4.7602	(001), <100> / <120>
α -Fe ₂ O ₃	R-3c (167)	a=5.007, c=13.641	(001), 5.007	(001), <100> / <120>
γ -Fe ₂ O ₃	P4 ₃ 32 (212)	a=8.33	(111), 11.78	(111), <-211> / <01-1>
Fe ₃ O ₄	Fd-3m (227)	a=8.378	(111), 11.85	(111), <-211> / <01-1>

Table II. Thermodynamic data used to calculate the Gibbs free energy change of the reaction from α -Fe₂O₃ to Fe₃O₄.³⁷

$\Delta_f G^0$ (T) J/(mol K)	$\Delta_f G^0 = \Delta_f H^0 - T\Delta_f S^0$
α -Fe ₂ O ₃	-824640 - T 87.4
Fe ₃ O ₄	-1115726 - T 146.14
$\Delta_f G^0$ (T)	80823 - 44.2 T

Table III. Thermodynamic data used to calculate the Gibbs free energy change.³⁷

	$\Delta_f H^0$ (kJ/mol)	$\Delta_f S^0$ (J/molK)
α -Fe ₂ O ₃	-824.640	87.4
Fe ₃ O ₄	-1115.726	146.14
O ₂	0.0	205.15

Table IV. The parameters found in fitting the time constants of the α -Fe₂O₃ (001)→Fe₃O₄ (111) transition using Arrhenius law

Pressure (Torr)	τ_0 (sec)	Activation energy (eV)
7.2×10^{-6}	$7.3 \pm 7.1 \times 10^{-7}$	2.0 ± 0.4
6.4×10^{-7}	$4.7 \pm 0.3 \times 10^{-9}$	2.5 ± 0.6
9.2×10^{-8}	$8.9 \pm 5.7 \times 10^{-9}$	2.6 ± 0.6

Figures and captions

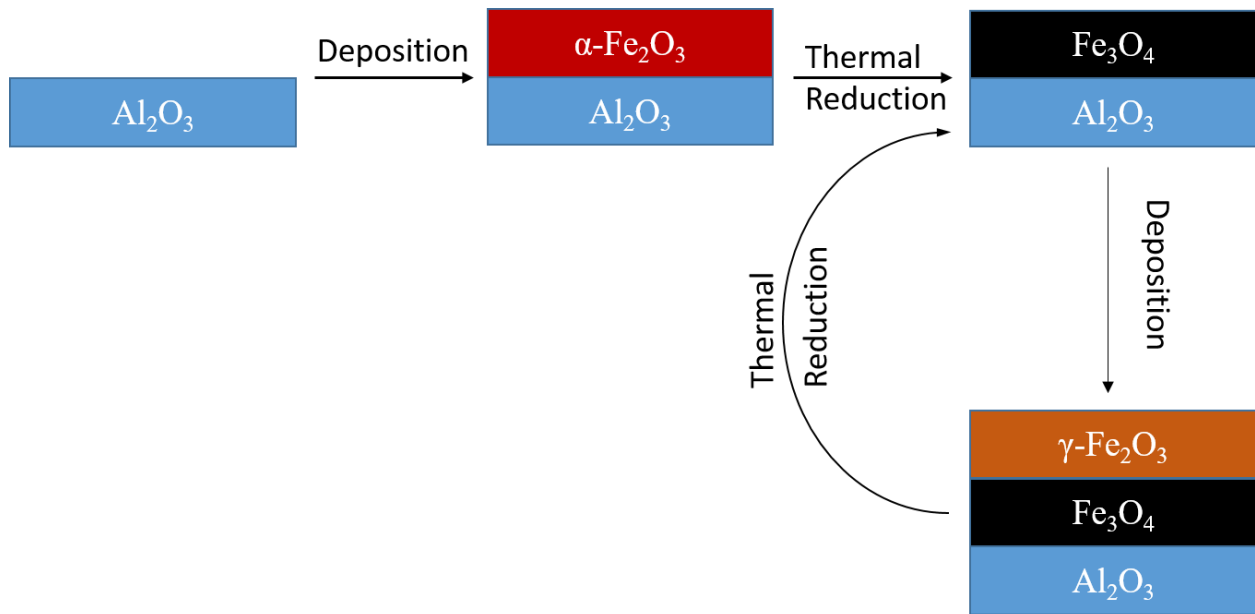


FIG 1 (color online). Schematic illustration of the deposition/thermal reduction processes to grow the Fe_3O_4 film.

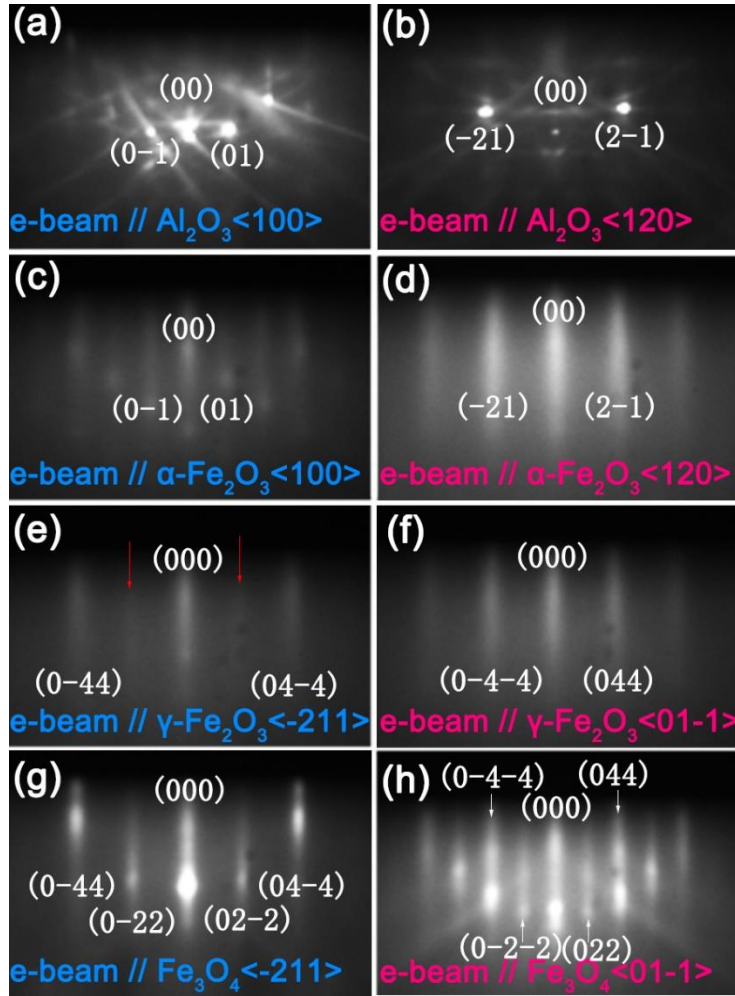


FIG 2 (color online). RHEED images of different surfaces with two different directions of incident electron beam. The diffraction streaks are marked using their corresponding reciprocal indices. (a) and (b) are the RHEED patterns of the Al_2O_3 (001) surface with e-beam parallel to Al_2O_3 $\langle 100 \rangle$ and $\langle 120 \rangle$. (c) and (d) are the RHEED patterns of the $\alpha\text{-Fe}_2\text{O}_3$ (001) with e-beam parallel to $\alpha\text{-Fe}_2\text{O}_3$ $\langle 100 \rangle$ and $\langle 120 \rangle$. (e) and (f) are the RHEED patterns of the $\gamma\text{-Fe}_2\text{O}_3$ (111) surface with e-beam parallel to $\gamma\text{-Fe}_2\text{O}_3$ $\langle -211 \rangle$ and $\langle 01-1 \rangle$. (g) and (h) are the RHEED patterns of the Fe_3O_4 (111) surface with e-beam parallel to Fe_3O_4 $\langle -211 \rangle$ and $\langle 01-1 \rangle$. The direction of the electron beam are the same for the images (a), (c), (e), and (g), and the same for the images (b), (d), (f), and (h).

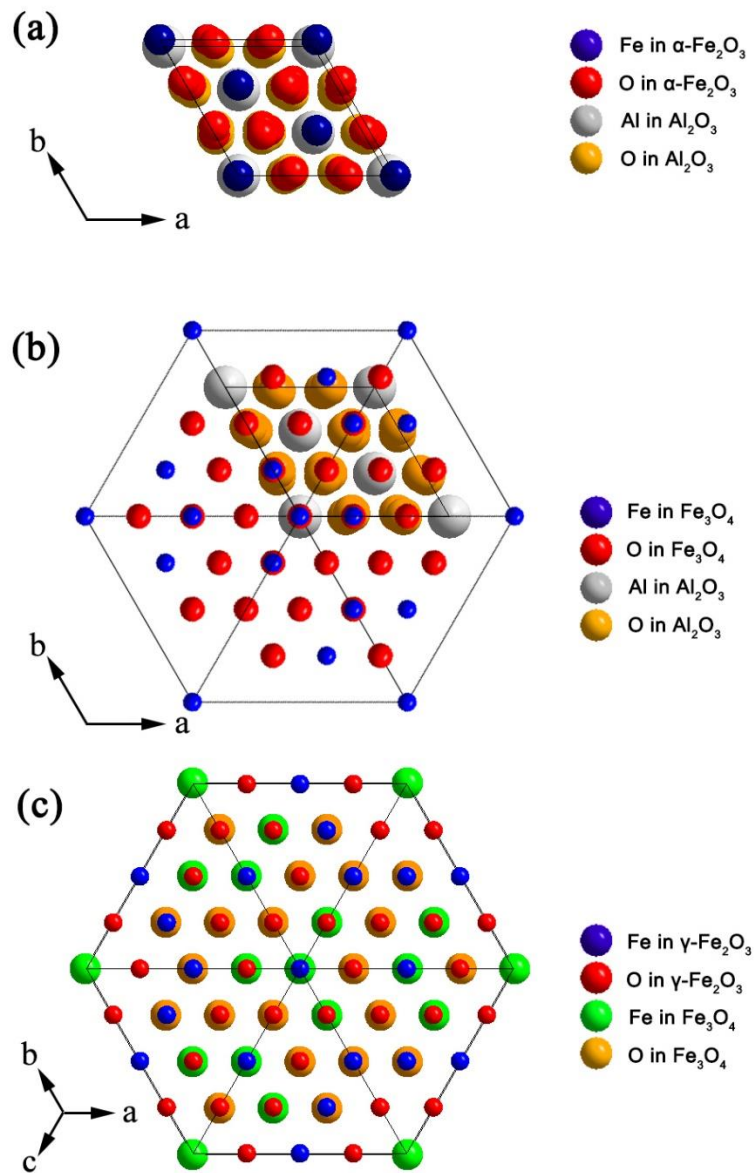


FIG 3 (color online). Schematics of the epitaxial relations. (a) Between Al_2O_3 (001) and $\alpha\text{-Fe}_2\text{O}_3$ (001). (b) Between Al_2O_3 (001) and Fe_3O_4 (111). (c) Between $\gamma\text{-Fe}_2\text{O}_3$ (001) and Fe_3O_4 (111).

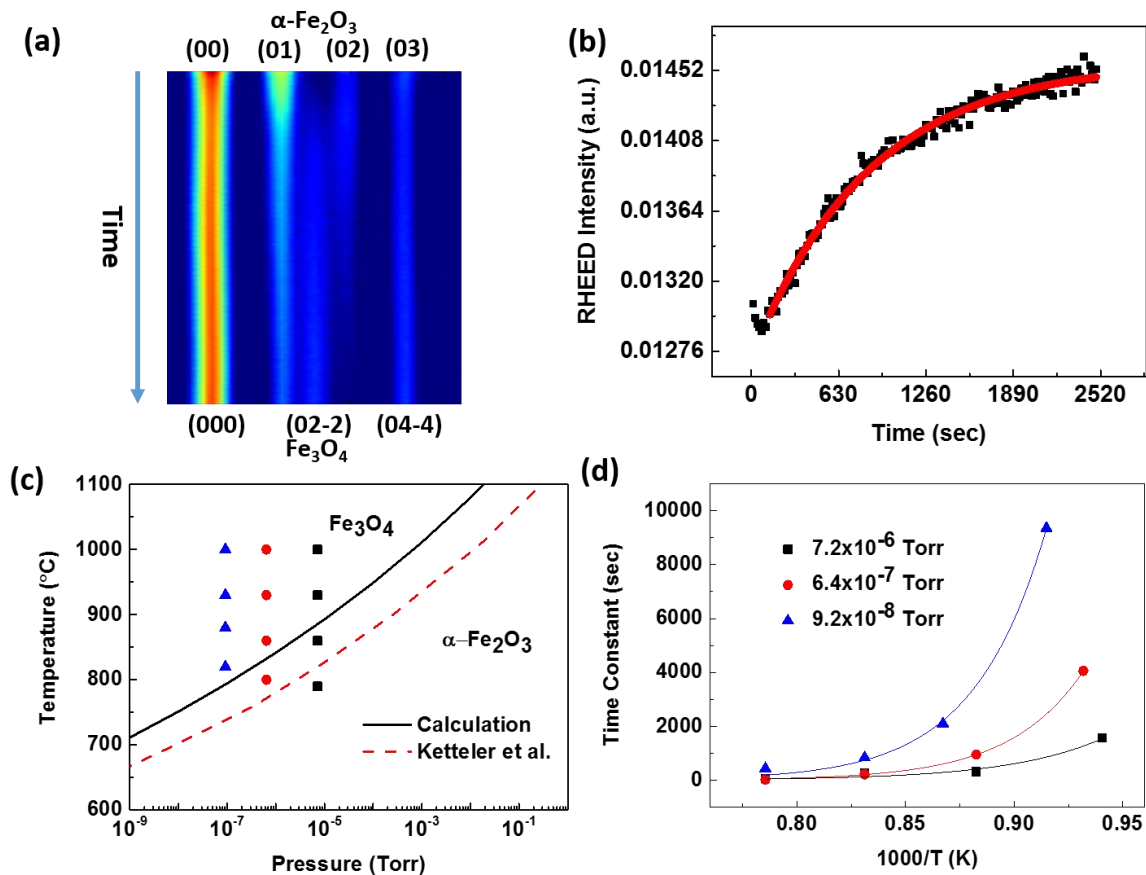


FIG 4 (color online). Thermal dynamics and kinetics of the $\alpha\text{-Fe}_2\text{O}_3$ (001) \rightarrow Fe_3O_4 (111) transition on the Al_2O_3 (001) substrates. (a) Time evolution of the RHEED pattern (see text) at 930 °C in 9.2×10^{-8} Torr O_2 . (b) The intensity of the Fe_3O_4 (02-2) streak as a function of time calculated from (a) and the fit (line). (c) The thermodynamic calculation of the phase boundary between $\alpha\text{-Fe}_2\text{O}_3$ and Fe_3O_4 and the conditions for the experimental measurements. The dashed line is the calculation from Ketteler et al.³⁸ (d) The temperature dependence of time constant of the $\alpha\text{-Fe}_2\text{O}_3$ (001) \rightarrow Fe_3O_4 (111) transition and the fit (lines) using the Arrhenius law.

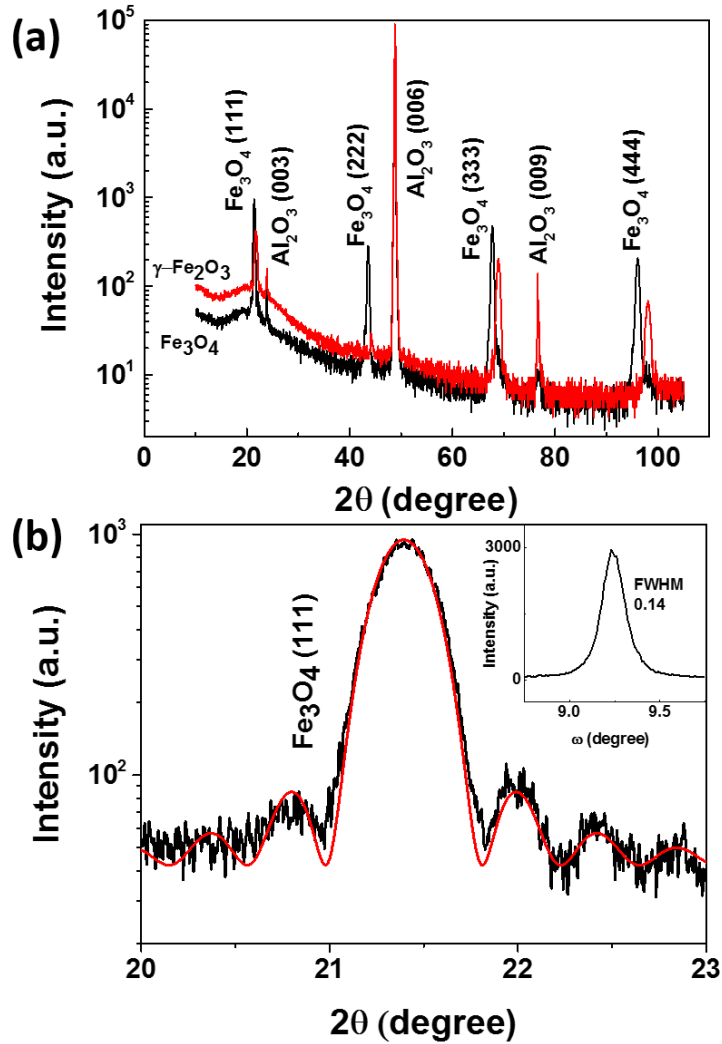


FIG 5 (color online). X-ray diffraction of the Fe_3O_4 film (~ 30 nm) as well as the annealed Fe_3O_4 film ($\gamma\text{-Fe}_2\text{O}_3$, see text). (a) Large range θ - 2θ scan using a cobalt K- α source ($\lambda=1.79$ Å). The indices of the $\gamma\text{-Fe}_2\text{O}_3$ peaks are the same as those of nearest Fe_3O_4 peaks. (b) The close-up view of the Fe_3O_4 (111) diffraction peak. The line is the fit of the Laue oscillation (see text). The inset is the rocking curve of the Fe_3O_4 (111) peak measured with a Cu K- α source ($\lambda=1.54$ Å). The full-width-half-maximum (FWHM) of the rocking curve is about 0.14 degree.

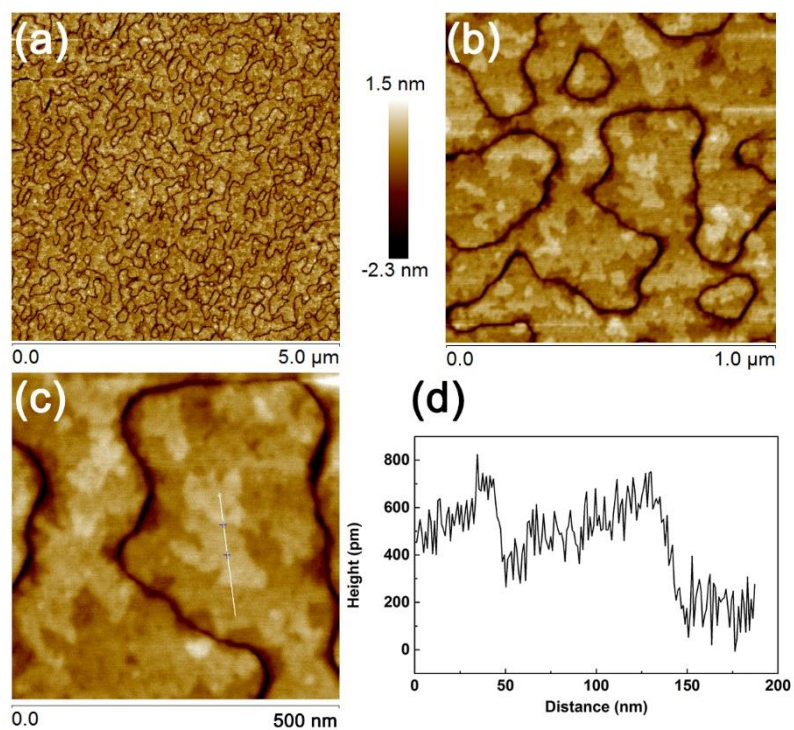


FIG 6 (color online). Surface morphology of the Fe_3O_4 film ($\sim 30 \text{ nm}$) measured using atomic force microscopy. (a) $5 \times 5 \mu\text{m}$. (b) $1 \times 1 \mu\text{m}$ and (c) $500 \times 500 \text{ nm}$. (d) A cross section of the film surface indicated by the line in (c).

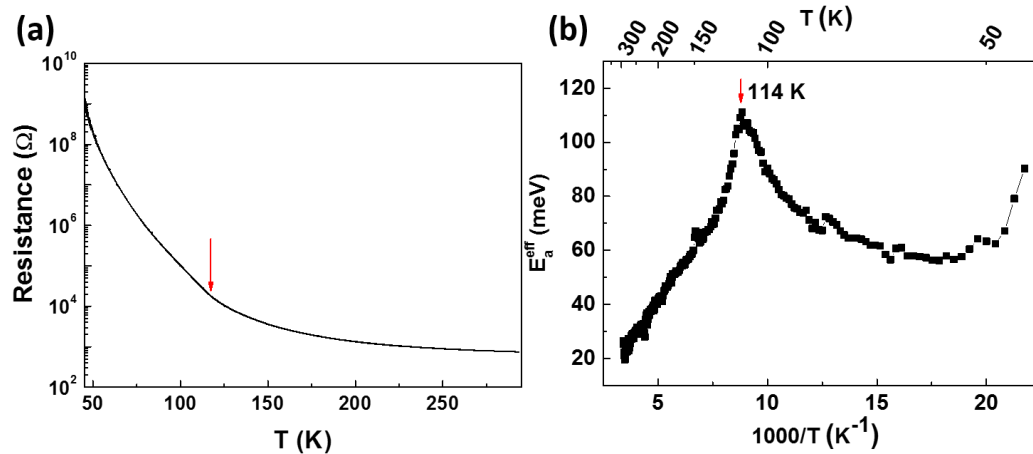


FIG 7 (color online). Temperature dependent electrical resistance (a) and the effective activation energy (b) (see text) of the Fe₃O₄ film (~30 nm). The Verwey transition is marked using the vertical arrows.

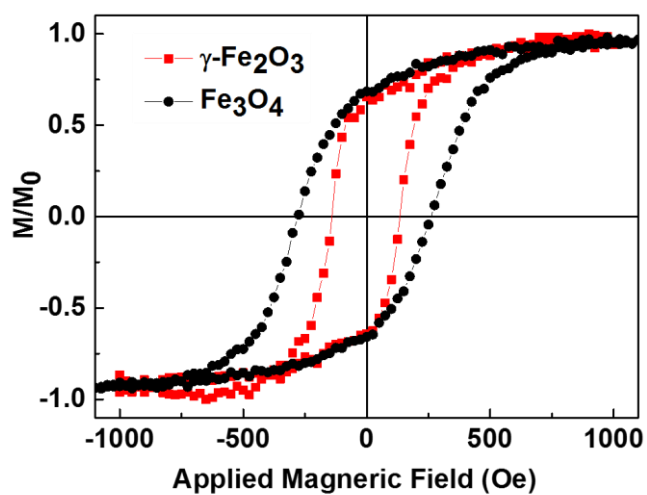


FIG 8 (color online). Magneto optical Kerr effect of the Fe_3O_4 film (~ 30 nm) and the $\gamma\text{-Fe}_2\text{O}_3$ film (from annealing a Fe_3O_4 film in O_2 , see text), measured at room temperature.

Supplementary materials

Kinetics and Intermediate Phases in Epitaxial Growth of Fe_3O_4 Films from Deposition and Thermal Reduction

Surface morphology of the Fe_3O_4 (111) films measured using atomic force microscopy (AFM)

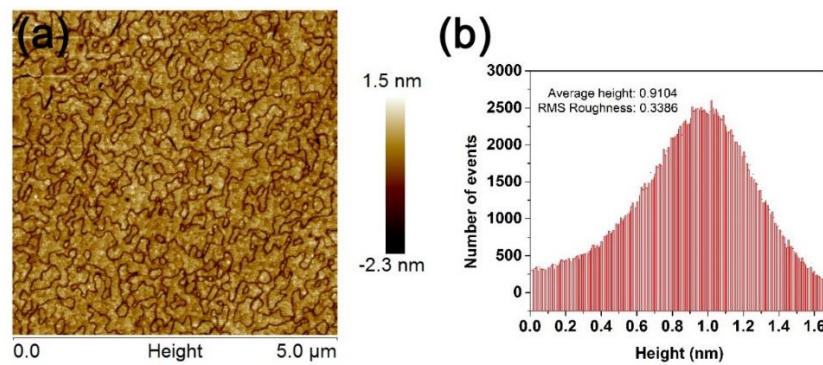


Figure S1. (a) AFM image of an Fe_3O_4 (111) film. (b) Height distribution and room-mean-square (RMS) roughness of the Fe_3O_4 (111) film.

Transition of the surface structure from the time evolution of the reflection high energy electron diffraction (RHEED) patterns

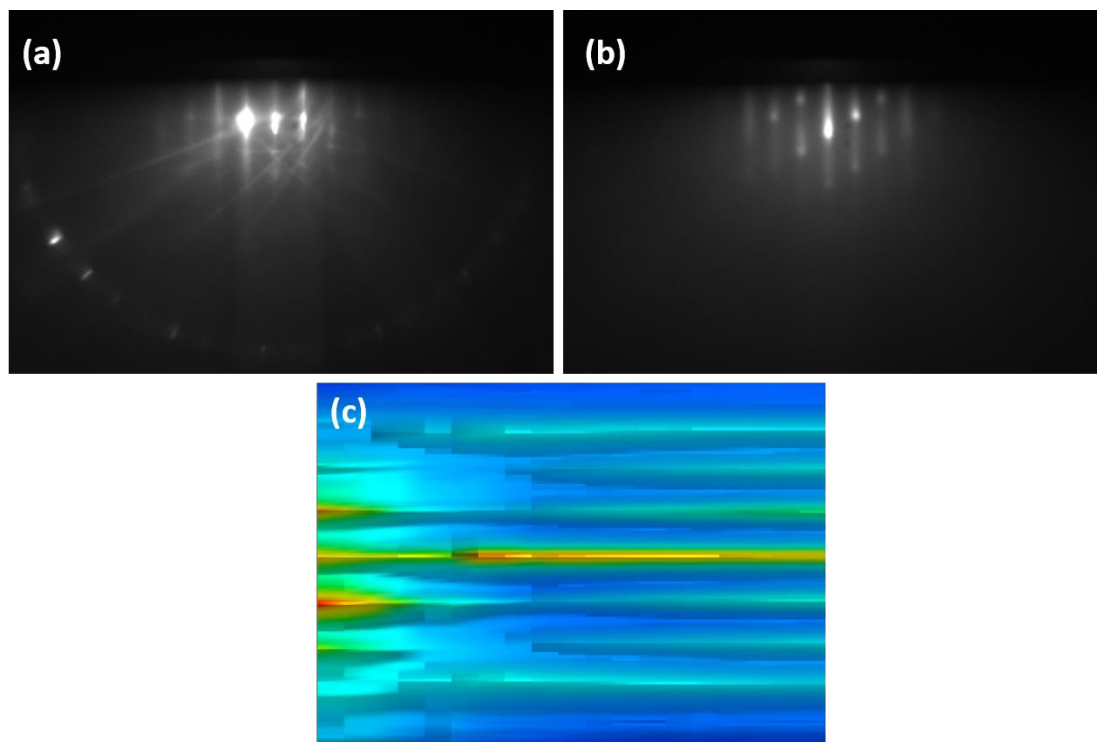


Figure S2. (a) RHEED pattern of the Al_2O_3 (001) substrate. (b) The RHEED pattern of $\alpha\text{-Fe}_2\text{O}_3$ (001) deposited on the Al_2O_3 substrate. (c) The RHEED evolution during the deposition. The horizontal axis is the time.

Figure S2 shows the time evolution of the RHEED pattern during the deposition of an $\alpha\text{-Fe}_2\text{O}_3$ layer on the Al_2O_3 (0001) substrate. The deposition started with a bare Al_2O_3 substrate, the RHEED pattern of which is shown in the Fig. S2 (a) with the incident e-beam along Al_2O_3 $\langle 100 \rangle$. The same diffraction pattern is shown in the Fig. 2(a) in the main text. After the deposition of a 2.5 nm Fe_2O_3 layer at 300 °C, the RHEED pattern becomes the one shown in Fig. S2(b), which is similar but with a different lattice constant, indicating a $\alpha\text{-Fe}_2\text{O}_3$ (001) layer. The evolution of the RHEED pattern during the deposition is shown in Fig. S2(c).

The evolution of the RHEED pattern (Fig. S2(c)) is obtained using the following procedure. 1) RHEED images are taken every 15 seconds. 2) A region of interest (ROI) containing the first order of the diffraction streaks is chosen (see Fig. S3). 3) The intensity of the ROI is integrated along the longer direction of the streaks to get a diffraction spectrum. 4) The diffraction spectra are plotted again time into a two dimensional image, to show the time evolution of the diffraction.

A clear transition of the surface from Al_2O_3 (0001) to Fe_2O_3 (001) can be visualize in the time evolution of the RHEED patterns. The time scale for the transition can also be analyzed.

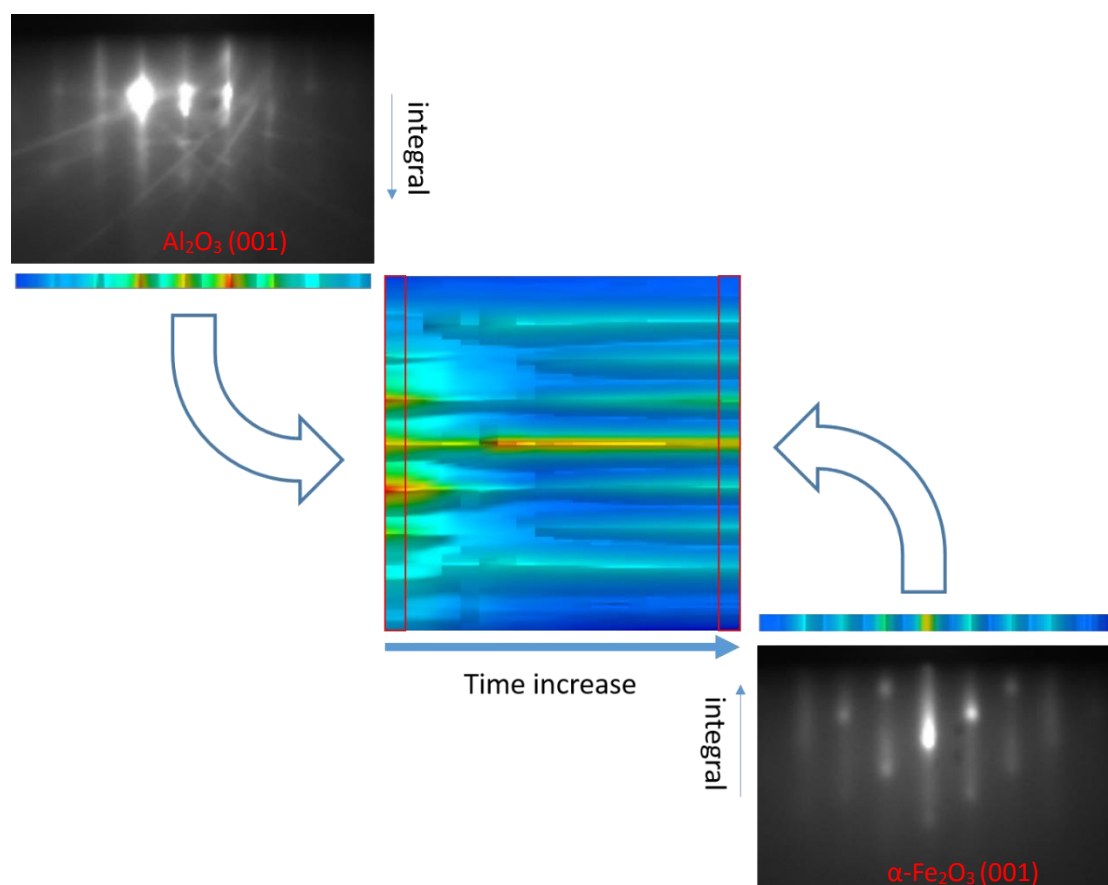


Figure S3. Schematic illustration of how to obtain the time evolution of the RHEED patterns

Comparison of the γ -Fe₂O₃ and Fe₃O₄ phases using the X-ray diffraction (XRD) measurements

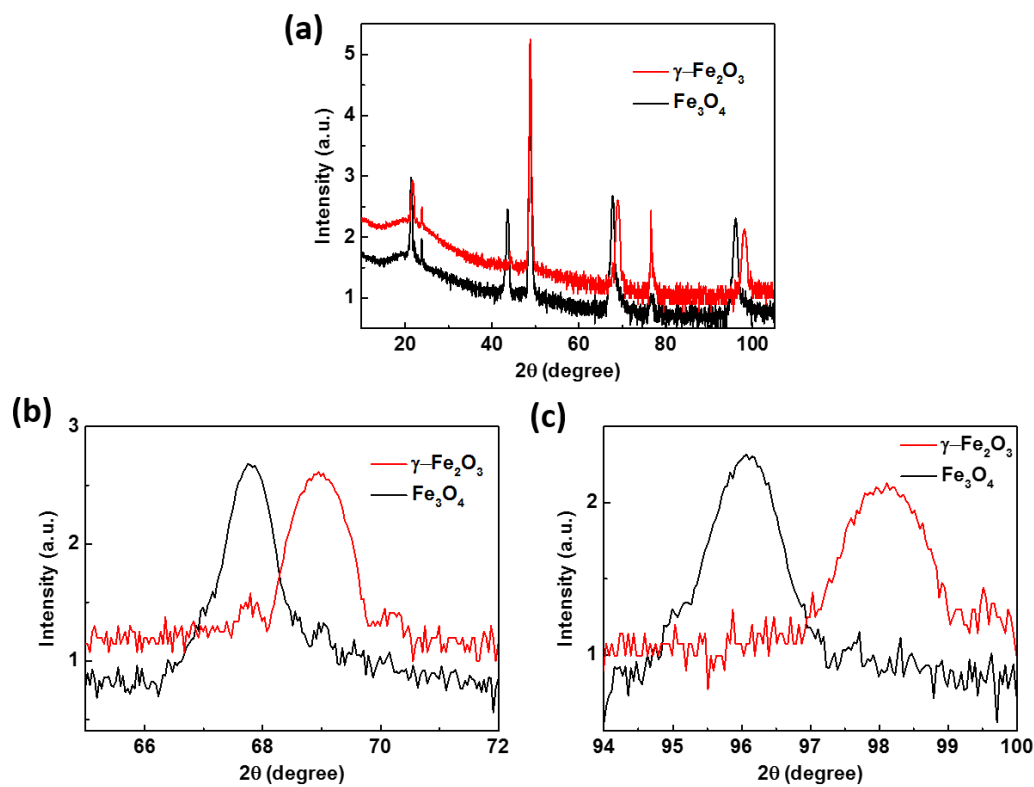


Figure S4. (a) The XRD spectra of Fe₃O₄ (111) and γ -Fe₂O₃ (111) films. (b) The close-up view of the spectra near the (333) (b) peak and the (444) peak (c) of Fe₃O₄ (111) and γ -Fe₂O₃ (111) films.

The similarity of the XRD spectra of the two films indicate similar crystal structures, which are the inverse spinel structure (space group = Fd-3m) and the cation deficient spinel structure for Fe₃O₄ and γ -Fe₂O₃ respectively. The lattice parameters are 8.378 Å and 8.33 Å for Fe₃O₄ and γ -Fe₂O₃ respectively. Because γ -Fe₂O₃ has a smaller lattice constant, the Bragg angles of the γ -Fe₂O₃ diffraction are larger than the corresponding angles of the Fe₃O₄ diffraction. According to Fig. S4(b) and S4(c), we can see the differences of the Bragg angles are 1.2 degree and 2.04 degree for the (333) and (444) peaks respectively.

Fe₃O₄ and γ -Fe₂O₃ d-spacing calculated from the X-ray diffraction measurements

Table S(I). Fe₃O₄ lattice parameters calculated from x-ray diffraction.

Peak/Plane	2θ (deg)	d (Å)	d₍₁₁₁₎ (Å)
(111)	21.432	4.811	4.811
(222)	43.592	2.409	4.818
(333)	67.752	1.605	4.814
(444)	96.072	1.203	4.812

Table S(II). γ -Fe₂O₃ lattice parameters calculated from x-ray diffraction.

Peak/Plane	2θ (deg)	d (Å)	d₍₁₁₁₎ (Å)
(111)	21.712	4.749	4.749
(222)	44.152	2.380	4.760
(333)	68.952	1.580	4.741
(444)	98.112	1.184	4.737

RHEED patterns of the γ -Fe₂O₃ (111) film obtained by annealing a Fe₃O₄ (111) film

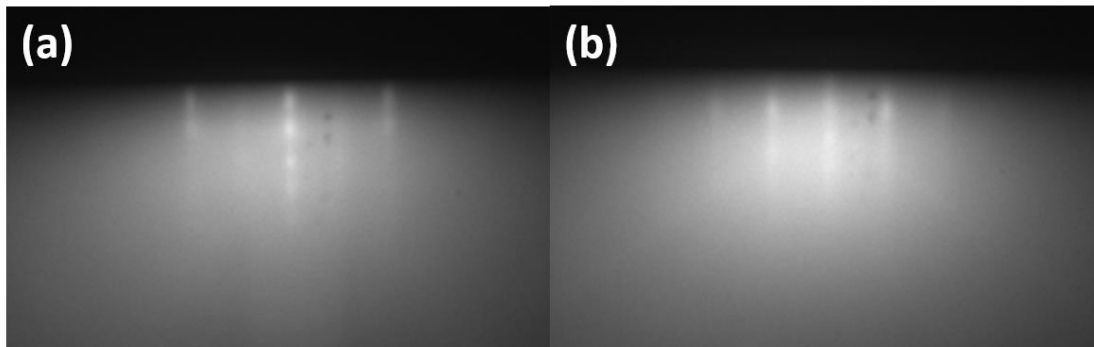


Figure S5. The RHEED pattern of a γ -Fe₂O₃ (111) film (from annealing a Fe₃O₄ (111) film) with the electron beam along $\langle -211 \rangle$ (a) and $\langle 01-1 \rangle$ (b) direction.

The RHEED pattern of the annealed film is similar to the RHEED pattern shown in Fig. 2(e) and 2(f) in the main text. These results indicate that the intermediate product during the deposition onto the Fe₃O₄ (111) surface is γ -Fe₂O₃ (111).

Derivation of Gibbs free energy change

Definition of symbols:

G : Gibbs free energy

$\Delta_f G$: formation Gibbs free energy. This is the Gibbs free energy of a compound relative to the corresponding elemental matters.

$\Delta_f G^0$: formation Gibbs free energy at standard condition ($P=1.0 \times 10^5$ Pa)

$\Delta_r G$: Gibbs free energy change for a reaction

$\Delta_r G^0$: Gibbs free energy change for a reaction at the standard condition

Consider the reaction: $\alpha - Fe_2O_3 \rightleftharpoons \frac{2}{3} Fe_3O_4 + \frac{1}{6} O_2$,

the Gibbs free energy change is $\Delta_r G = \left(\frac{2}{3} G_{Fe_3O_4} + \frac{1}{6} G_{O_2}\right) - G_{Fe_2O_3}$.

Since $G_{Fe_2O_3}$, $G_{Fe_3O_4}$, and G_{O_2} are not generally available, we will try to derive their relation to the values at the standard condition.

From

$$G_{Fe_2O_3} = \Delta_f G_{Fe_2O_3} + 2G_{Fe} + \frac{3}{2} G_{O_2}$$

$$G_{Fe_3O_4} = \Delta_f G_{Fe_3O_4} + 3G_{Fe} + 2G_{O_2},$$

one finds

$$\begin{aligned} \Delta_r G &= \left[\frac{2}{3} (\Delta_f G_{Fe_3O_4} + 3G_{Fe} + 2G_{O_2}) + \frac{1}{6} G_{O_2} \right] - (\Delta_f G_{Fe_2O_3} + 2G_{Fe} + \frac{3}{2} G_{O_2}) \\ &= \frac{2}{3} \Delta_f G_{Fe_3O_4} - \Delta_f G_{Fe_2O_3}. \end{aligned}$$

Now we look at,

$$\Delta_f G_{Fe_3O_4} = \Delta_f G_{Fe_3O_4}^0 + (G_{Fe_3O_4} - G_{Fe_3O_4}^0) - 3(G_{Fe} - G_{Fe}^0) - 2(G_{O_2} - G_{O_2}^0).$$

Since for solid state matters, the Gibbs free energy is not affected by the pressure very much, one can assume $G_{Fe_3O_4} - G_{Fe_3O_4}^0 = 0$ and $G_{Fe} - G_{Fe}^0 = 0$. Therefore, it follows from that

$$\Delta_f G_{Fe_3O_4} = \Delta_f G_{Fe_3O_4}^0 - 2(G_{O_2} - G_{O_2}^0).$$

Similarly, one has $\Delta_f G_{Fe_2O_3} = \Delta_f G_{Fe_2O_3}^0 - \frac{3}{2}(G_{O_2} - G_{O_2}^0)$.

Now the Gibbs free energy change of the reaction becomes

$$\begin{aligned} \Delta_r G &= \frac{2}{3} [\Delta_f G_{Fe_3O_4}^0 - 2(G_{O_2} - G_{O_2}^0)] - [\Delta_f G_{Fe_2O_3}^0 - \frac{3}{2}(G_{O_2} - G_{O_2}^0)] = \frac{2}{3} \Delta_f G_{Fe_3O_4}^0 + \\ &\frac{1}{6} (G_{O_2} - G_{O_2}^0) - \Delta_f G_{Fe_2O_3}^0. \end{aligned}$$

If the O_2 is treated as an ideal gas, then the molar Gibbs free energy change is $G_{O_2} - G_{O_2}^0 = RT \ln \left(\frac{P}{P_0}\right)$, where $P_0 = 1.0 \times 10^5$ Pa is the pressure at standard condition.

Hence, one reaches the relation: $\Delta_r G = \frac{2}{3} \Delta_f G_{Fe_3O_4}^0 - \Delta_f G_{Fe_2O_3}^0 + \frac{1}{6} RT \ln \left(\frac{P}{P_0}\right)$.

Calculation of Gibbs free energy change at standard condition

Table S(III). Data for calculating the Gibbs free energy change.¹

	$\Delta_f H^0$ (kJ/mol)	$\Delta_f S^0$ (J/mol K)
$\alpha\text{-Fe}_2\text{O}_3$	-824.640	87.4
Fe_3O_4	-1115.726	146.14
O_2	0.0	205.15

$$\begin{aligned}\Delta_r G^0(T) &= \Delta_r H^0 - T\Delta_r S^0 \\ &= \left(\frac{2}{3} \Delta_f H_{\text{Fe}_3\text{O}_4}^0 + \frac{1}{6} \Delta_f H_{\text{O}_2}^0 - \Delta_f H_{\text{Fe}_2\text{O}_3}^0 \right) \\ &\quad - T \left(\frac{2}{3} \Delta_f S_{\text{Fe}_3\text{O}_4}^0 + \frac{1}{6} \Delta_f S_{\text{O}_2}^0 - \Delta_f S_{\text{Fe}_2\text{O}_3}^0 \right) \\ &= \left(\frac{2}{3} \times (-1115726) + \frac{1}{6} \times 0 + 824640 \right) \\ &\quad - T \left(\frac{2}{3} \times 146.14 + \frac{1}{6} \times 205.15 - 87.4 \right) \\ &= (80823 - 44.2 T) \text{ J/mol}\end{aligned}$$

The crystallite size in the out-of-plane direction of a Fe₃O₄ (111) film

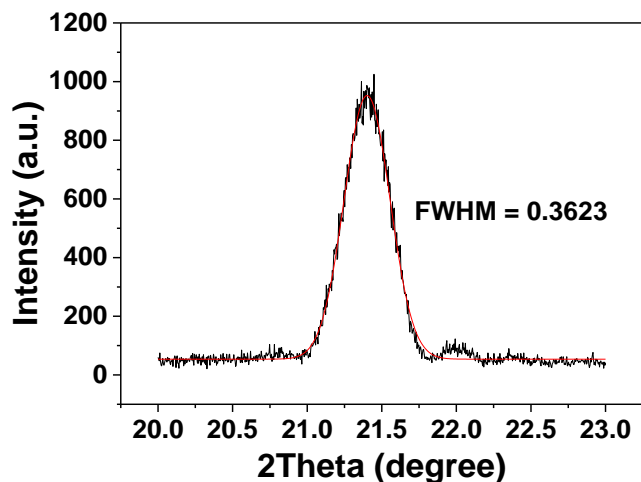


Figure S6. The (111) peak of the Fe₃O₄ thin film.

The size of the crystallites can be estimated using the Scherrer equation² $\tau = \frac{K\lambda}{\beta \cos(\theta)}$, where τ is the mean size of the crystalline domains, K is a dimensionless shape factor (taken as 0.9), λ is the X-ray wavelength, β is width of the diffraction peak (FWHM) in radians, and θ is the Bragg angle.

According to Fig. S6, one finds

$$\tau = \frac{K\lambda}{\beta \cos(\theta)} = \frac{0.9 * 1.79}{0.3623 * \pi/180 * \cos(21.4015/2 * \pi/180)} = 259.3 \text{ \AA}.$$

The crystallite size of the in-plane direction of Fe₃O₄ (111)

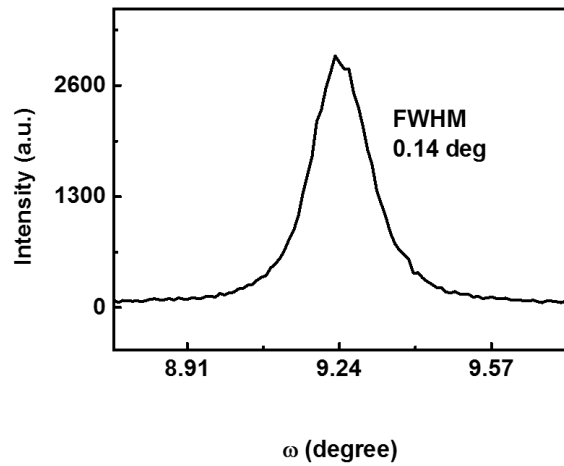


Figure S7. The rocking curve of the Fe₃O₄ thin film.

Using Scherrer equation $\tau = \frac{K\lambda}{\beta \cos(\theta)}$, one finds,

$$\tau = \frac{K\lambda}{\beta \cos(\theta)} = \frac{0.9 * 1.54}{0.14 * \pi/180 * \cos(9.2309 * \pi/180)} = 574.7 \text{ \AA}.$$

References

- ¹ R.A. Robie and B.S. Hemingway, *Thermodynamic Properties of Minerals and Related Substances at 298.15 K and 1 Bar (105 Pascals) Pressure and at Higher Temperatures* (U.S. G.P.O. ; For sale by U.S. Geological Survey, Information Services, Washington; Denver, CO, 1995).
- ² B.D. Cullity, *Elements of X-Ray Diffraction*. (Addison-Wesley Pub. Co., Reading, Mass., 1956).